Multiphysics Analysis and Simulation of Wireless Passive Temperature and Pressure Sensors for Harsh-Environment Applications

Yijia Cheng, *Graduate Student Member, IEEE*, Yujie Hua, *Graduate Student Member, IEEE*, Baiyun Wang, Kang Wang, Wenxuan Tang, *Member, IEEE*, Gang Shao, and Wei E. I. Sha, *Senior Member, IEEE*

***Abstract*—Monitoring temperature and pressure in harsh environments is vital for industrial applications. This study presents a comprehensive multiphysics analysis and simulation of wireless passive temperature and pressure sensors, providing a feasible research framework for accurate simulation model development tailored to these devices and applications. The analysis focuses on evaluating the electromagnetic-thermal-mechanical coupling effects and improving the accuracy of sensor modeling under extreme environments. In particular, multiphysics simulations are performed on a pressure sensor that incorporates structural deformations induced by thermal expansion and external pressure. Comparison with available experimental data demonstrates significantly enhanced accuracy compared with conventional simple models, yielding a resonance frequency deviation of 0.32% (vs. 2.65%) and an error in the S_{11} parameter estimation of 13.15% (vs. 101.92%) relative to measurements. These findings underscore the importance of accounting for multiphysics coupling in sensor design and provide insights for performance optimization in harsh environments.**

***Index Terms*—Passive wireless sensors, metamaterial sensors, multiphysics simulation, temperature sensor, pressure sensor, harsh environments.**

I. Introduction

WIRELESS passive sensors for high-temperature and high-pressure environment monitoring are essential to aeronautics [1], automobiles [2] and industrial applications such as gas turbines [3], [4]. In harsh environments, accurate monitoring of temperature and pressure is essential for ensuring system reliability and operational safety. Temperature measurement helps prevent failures induced by excessive heat, while pressure monitoring enables control of the air-fuel mixture to reduce engine stall risks and achieve optimal pressure ratios for maximum thermal efficiency during turbine operations [4]. Compared with traditional wired or battery-powered sensors, wireless passive sensors offer simpler configurations, higher reliability, and lower maintenance costs in high-temperature environments. Their capability for remote and real-time signal transmission also makes them particularly suitable for monitoring extreme environmental conditions [5]. With advances in high-temperature-resistant materials such as silicon carbide [6], polycrystalline diamond, and polymer-derived ceramics (PDCs) [7], [8], [9], sensor performance in extreme temperature, pressure, and vibration conditions has been significantly improved. However, these materials often exhibit variations in dielectric properties with temperature or pressure [10], leading to strong coupling among electromagnetic, thermal, and mechanical fields within the sensor. Understanding and accurately modeling such multiphysics interactions is therefore essential for optimizing sensor design and ensuring reliable operation in harsh environments.

In recent years, progress in microwave technology has driven extensive research on multiphysics modeling, leading to various simulation approaches for complex coupled systems [11], [12], [13], [14], [15], [16]. Typically, wireless passive sensors are analyzed using electromagnetic (EM) models based on Maxwell's equations or equivalent circuit representations, where sensing mechanisms rely on the resonant frequency shifts of the resonators induced by environmental parameter variations [17], [18], [19], [20], [21], [22], [23]. For temperature sensors, EM simulations commonly represent thermal effects by assigning temperature-dependent dielectric properties to materials, allowing evaluation of resonance or scattering responses under varying conditions [24], [25]. For pressure sensors, structural deformation is generally obtained from mechanical analyses (e.g., thin-plate or large-deflection theory) [26] and then approximated in EM simulations by modifying relevant geometric parameters [27], [28], [29], [30], [31], [32]. Consequently, most existing studies on microwave sensors in harsh environments treat electromagnetic, thermal, and mechanical domains independently, lacking a unified multiphysics framework that captures their coupled interactions in wireless passive sensor modeling. Despite the computational advantages of simplified EM models, intrinsic electromagnetic-thermal-mechanical couplings remain insufficiently addressed, underscoring the need for

Received 21 October 2025; accepted 30 November 2025. Date of publication 9 December 2025; date of current version 24 December 2025. This work was supported by the National Key Research and Development Program of China under Grant 2021YFB3200502. *(Corresponding author: Wei E. I. Sha.)*

Yijia Cheng and Wei E. I. Sha are with the College of Information Science and Electronic Engineering, Zhejiang University, Hangzhou 310027, China (e-mail: 12131036@zju.edu.cn; weisha@zju.edu.cn).

Yujie Hua, Baiyun Wang, and Wenxuan Tang are with the State Key Laboratory of Millimeter Waves, School of Information Science and Engineering, Southeast University, Nanjing 210096, China (e-mail: yujiehua@seu.edu.cn; 220230735@seu.edu.cn; wenxuant@seu.edu.cn).

Kang Wang and Gang Shao are with the School of Materials Science and Engineering, Zhengzhou University, Zhengzhou 450001, China (e-mail: kangwang_zzu@163.com; gang_shao@zzu.edu.cn).

Digital Object Identifier 10.1109/JMMCT.2025.3641976

rigorous evaluation and validation for specific sensor models and operating conditions to ensure accurate simulation-experiment consistency.

Building on existing multiphysics modeling and co-simulation approaches [33], [34], [35], [36], [37], this study develops EM-thermal-mechanical multiphysics models with appropriate simplifications to balance computational efficiency and accuracy, specifically for wireless passive temperature and pressure sensors operating in harsh environments. The main contributions are as follows: (1) An in-depth analysis of the coupling mechanisms among EM, thermal, and mechanical fields in high-temperature and high-pressure microwave sensor systems is presented, establishing a unified and adaptable multiphysics framework applicable to various coupling scenarios. (2) The significance of multiphysics simulation over conventional EM modeling is systematically evaluated, offering insights into model optimization and error assessment for sensor design and measurement. (3) An enhanced pressure sensor model is proposed, incorporating structural deformations induced by thermal expansion and external pressure, which markedly improves simulation accuracy compared with the simple models.

The remainder of this paper is organized as follows. Section II reviews the governing equations of the three physical fields and corresponding boundary conditions in the sensor system, and subsequently establishes the complete EM-thermal-mechanical coupling model with constitutive relations. Section III presents the multiphysics simulation of a spiral electromagnetic resonator, serving as a representative metamaterial-based temperature sensor, to analyze coupling effects and assess their significance. Section IV extends the analysis to a pressure sensor with a sealed cavity and deformable diaphragms. Finally, Section V concludes by summarizing the modeling framework and simplification strategies for multiphysics sensor systems.

II. Governing Equations and Coupled EM-Thermal-Mechanical Model of Sensors

To analyze the coupling between different physical fields, it is essential to establish the governing equations for each domain and define boundary conditions adapted to the device structure and operating environment. The three fields are interrelated through corresponding physical quantities in both the governing equations and boundary conditions, as described in Sections II-A, II-B, and II-C, and summarized in Section II-D.

A. Electromagnetic Analysis for Passive Wireless Sensors

The electromagnetic (EM) response of a wireless sensor, characterized by its scattering parameters (S-parameters), is governed by Maxwell's equations in both the time and frequency domains:

$$\nabla \times \mathbf{E} = -\frac{\partial \mathbf{B}}{\partial t} \xrightarrow{time-harmonic} \nabla \times \widetilde{\mathbf{E}} = -j\omega\widetilde{\mathbf{B}}, \tag{1}$$

$$\nabla \times \mathbf{H} = \mathbf{J} + \frac{\partial \mathbf{D}}{\partial t} \xrightarrow{time-harmonic} \nabla \times \widetilde{\mathbf{H}} = \tilde{\mathbf{J}} + j\omega\widetilde{\mathbf{D}}, \tag{2}$$

$$\nabla \cdot \mathbf{D} = \boldsymbol{\rho} \xrightarrow{time-harmonic} \nabla \cdot \tilde{\mathbf{D}} = \tilde{\boldsymbol{\rho}}, \tag{3}$$

$$\nabla \cdot \mathbf{B} = 0 \xrightarrow{time-harmonic} \nabla \cdot \tilde{\mathbf{B}} = 0, \tag{4}$$

where symbol with tilde (e.g., $\widetilde{\mathbf{E}}$, $\widetilde{\mathbf{H}}$, etc.) is phasor representation of a time-harmonic quantity (e.g. $\mathbf{E}(\mathbf{r},t) = \Re e[\widetilde{\mathbf{E}}(\mathbf{r})e^{j\omega t}]$, $\mathbf{H}(\mathbf{r},t) = \Re e[\widetilde{\mathbf{H}}(\mathbf{r})e^{j\omega t}]$), and ω is the angular frequency of the time-harmonic field.

To simulate a device's scattering spectra accurately, three essential factors must be considered: the incident field (i.e., source), material properties (i.e., constitutive parameters), and structural configuration (i.e., boundary conditions). These electromagnetic characteristics (e.g., permittivity $\varepsilon(T,P)$, permeability μ, conductivity σ, and structural dimensions) are iteratively updated according to thermal and mechanical field distributions in multiphysics simulation to reflect realistic operating conditions.

B. Heat Conduction in Sensors

The governing equation (i.e., thermal conduction equation) for transient thermal analysis is

$$\rho c_p(T)\frac{\partial T}{\partial t} - \nabla \cdot (\kappa(T)\nabla T) = Q, \tag{5}$$

and the corresponding steady-state conduction is

$$\nabla \cdot (\kappa(T)\nabla T) = -Q, \tag{6}$$

where ρ denotes the density of the material, $c_p(T)$ the specific heat coefficient (function of temperature), $\kappa(T)$ the thermal conductivity (function of temperature), and Q the heat source. Coupling the EM field with thermal field, the EM heating (i.e., dissipated electromagnetic power)

$$Q_{\text{em}} = \frac{1}{2}\,\text{Re}\,(\mathbf{J}\cdot\mathbf{E}^*) \tag{7}$$

is introduced into the heat source Q, where J is the conduction current. Considering that the model geometry changes (e.g., due to structural deformation) when incorporating stress fields, an additional term should be included in these equations:

$$\begin{aligned}\rho c_p\frac{\partial T}{\partial t} + \rho c_p\mathbf{u}\cdot\nabla T + \nabla\cdot(\kappa\nabla T) = Q\\ \xrightarrow{steady-state} \rho c_p\mathbf{u}\cdot\nabla T + \nabla\cdot(\kappa\nabla T) = Q\end{aligned} \tag{8}$$

where $\mathbf{u}$ (SI unit: m/s) is the velocity field defined by the translational motion subnode (which is contained in the mesh node of simulation). And the contribution $\rho c_p\mathbf{u}\cdot\nabla T$ describes the effect of a moving coordinate system.

In sensor systems, the thermal boundary conditions are primarily determined by the device and its surrounding environment. When the sensor is attached to a target surface, heat conducts from the object through the sensor's base and exchanges with the environment via convection (between the device surface and air) and radiation (from surrounding high-temperature objects). These mechanisms define the convective boundary conditions, i.e.,

$$-\hat{n}\cdot\kappa\nabla T = h\,(T - T_{\text{sur}})\,, \tag{9}$$

and radiative boundary conditions, i.e.,

$$-\hat{n}\cdot\kappa\nabla T=\varepsilon_{\mathrm{e}}\sigma_{\mathrm{e}}\left(T^4-T_{\mathrm{sur}}^4\right), \tag{10}$$

for the thermal conduction equation, where h is the convective heat transfer coefficient, ε_{e} refers to the emissivity of the medium surface, $\sigma_{\mathrm{e}}=5.68\times10^{-8}\,\mathrm{W/m^2}\,K^4$ is the Stefan-Boltzmann constant, T_{sur} refers to the surrounding temperature, and $\hat{n}$ represents the normal unit vector relative to the device surface. The left-hand side of these equations represents the normal heat flux across the boundary, i.e., the temperature gradient scaled by thermal conductivity. Accordingly, the heat transfer boundary conditions at surfaces exposed to air or other external fluids can be directly derived from (9) and (10) as

$$-\kappa(T)\frac{\partial T}{\partial n}=h\left(T-T_{\mathrm{sur}}\right)+\varepsilon_{\mathrm{e}}(T)\sigma\left(T^4-T_{\mathrm{sur}}^4\right). \tag{11}$$

The bottom surface of the device is in direct contact with the measured object, enabling solid-to-solid heat conduction. Consequently, the temperature at the device bottom satisfies the Dirichlet boundary condition, i.e.,

$$T=T_{\mathrm{o}} \tag{12}$$

where T_{o} denotes the temperature of the object to which the sensor is attached. In another sensing scenario, when the sensor is suspended in a fluid environment (e.g., air or liquid) rather than attached to a solid surface, it measures the temperature of the surrounding fluid. In this case, heat transfer occurs primarily through convection, and the convective boundary condition given in (11) is applied to all device surfaces.

Transient heat conduction analysis is primarily relevant for high-power active devices. For the present passive sensor system, the internal temperature distribution can be obtained by solving the steady-state heat conduction equation (6), which is analogous to Poisson's equation in electrostatics, where heat sources correspond to charges, temperature to potential, and thermal conductivity to permittivity. Because heat conduction occurs on a much slower time scale than electromagnetic oscillations, the microwave heat source derived from EM simulations is treated as a time-averaged quantity over the thermal time scale Δt to solve the coupled EM-thermal governing equation.

C. Stress and Strain of Sensors

The deformation of a body per unit length or volume is represented by the strain tensor, defined as

$$\overline{s}=\frac{1}{2}\left(\nabla\mathbf{u}+(\nabla\mathbf{u})^T\right) \tag{13}$$

where $\mathbf{u}$ is the displacement vector field of each point on the device surface relative to its initial position, i.e., $\mathbf{u}(\mathbf{r})=\mathbf{r}-\mathbf{r}_0$. The tensor $\bar{s}$ is a second-order (3×3) strain tensor that contains nine components in a three-dimensional coordinate system. The three diagonal components correspond to the normal strains, expressed as $s_{ii}=u/L$, where L denotes the initial length. The remaining six off-diagonal components represent shear strains, calculated as [38]

$$\overline{s}_{ij}=\frac{1}{2}\left[\frac{\partial u_j}{\partial x_i}+\frac{\partial u_i}{\partial x_j}\right]\quad(i,j\Rightarrow x,y,z\text{ directions}). \tag{14}$$

The elastic wave equation establishes the relationship among the internal stress, structural deformation (i.e., boundary displacement), and the applied external pressure, and can be expressed as:

$$\rho\frac{\partial^2\boldsymbol{u}}{\partial t^2}+\gamma\frac{\partial\boldsymbol{u}}{\partial t}=\nabla\cdot\overline{\boldsymbol{\sigma}}+\boldsymbol{f}_{\mathrm{e}} \tag{15}$$

where ρ is the density of the material, γ is the damping coefficient, $\boldsymbol{f}_{\mathrm{e}}$ is the external force generated by the environmental air pressure, and $\overline{\boldsymbol{\sigma}}$ is the stress tensor which displays the internal force per unit area of the material in all directions of the coordinate system and can be expressed in matrix form for an isotropic linear elastic solid as

$$\overline{\boldsymbol{\sigma}}=\begin{bmatrix}\sigma_{xx}&\tau_{xy}&\tau_{xz}\\\tau_{xy}&\sigma_{yy}&\tau_{yz}\\\tau_{xz}&\tau_{yz}&\sigma_{zz}\end{bmatrix}, \tag{16}$$

where the diagonal elements represent the normal stress components and the off-diagonal elements correspond to the shear stress components.

For the steady-state analysis, this wave equation reduces to:

$$-\nabla\cdot\overline{\boldsymbol{\sigma}}=\boldsymbol{f}_{\mathrm{e}}. \tag{17}$$

The equilibrium condition requires the stress tensor to be symmetric, i.e., $\sigma_{ij}=\sigma_{ji}$, making it a rank-two symmetric tensor with only six independent components.

The constitutive relationship between stress and strain in a linear elastic material is given by

$$\overline{\boldsymbol{\sigma}}=\overline{\mathbf{C}}:\overline{\boldsymbol{s}}\xrightarrow{component}\overline{\sigma}_{ij}=\overline{C}_{ijkl}\cdot\overline{s}_{kl} \tag{18}$$

where $\overline{\mathbf{C}}$ denotes the rank-four elasticity tensor. For practical computation, it is often expressed in Voigt notation as a 6×6 stiffness matrix that relates the stress and strain column vectors (each of size 6×1) composed of their six independent components.

The coupling between the mechanical governing equation (18) and the electromagnetic field is described by the stress-charge constitutive relations (or equivalently, the strain-charge form) for piezoelectric materials:

$$\overline{\sigma}_{ij}=\overline{C}_{ijkl}\overline{s}_{kl}-\overline{e}_{ijk}^{T}E_k \tag{19a}$$

$$\overline{D}_i=\overline{e}_{ijk}\overline{s}_{jk}+\varepsilon_0\overline{\varepsilon}_{ij}E_j \tag{19b}$$

where $\overline{e}$ denotes the piezoelectric coupling tensor and $\overline{\varepsilon}$ is the relative permittivity tensor. Piezoelectric materials exhibit both the direct piezoelectric effect (generation of electric charge under mechanical stress) and the inverse piezoelectric effect (generation of mechanical stress under an applied electric field), thereby establishing a bidirectional coupling between the mechanical and electromagnetic fields.

For thermal expansion effects induced by heat flow, the strain terms in the constitutive relation (18) can be modified as

$$\overline{\sigma}_{ij}=\overline{C}_{ijkl}\cdot\left[\overline{s}_{kl}+d(T)\overline{\delta}_{kl}\left(T-T_{ref}\right)\right], \tag{20}$$

where $d(T)$ represents the coefficient of thermal expansion, $\overline{\delta}_{kl}$ denotes the Dirac delta function, and T_{ref} refers to the

reference temperature of the initial state. Therefore, the comprehensive analysis of EM-thermal-mechanical multiphysics model of piezoelectric materials can be written as

$$\overline{\sigma}_{ij} = \overline{C}_{ijkl}\left[\overline{s}_{kl} + d(T)\overline{\delta}_{kl}\left(T - T_{\text{ref}}\right)\right] - \overline{e}_{ijk}E_k \tag{21}$$

$$\overline{D}_i = \overline{e}_{ijk}\left[\overline{s}_{jk} + d(T)\overline{\delta}_{jk}\left(T - T_{\text{ref}}\right)\right] + \overline{\varepsilon}_{ij}(T)E_j, \tag{22}$$

where the thermal expansion term (20) is incorporated into the stress–charge constitutive equations (19), and the dielectric permittivity is temperature-dependent. For wireless passive sensors, piezoelectric materials are rarely used as substrates, as the electric charge generated by piezoelectric effects is significant only under very low-frequency EM fields (e.g., electrostatic fields).

For mechanical simulations in sensor systems, the boundary conditions of the elastic wave equation are determined by the device's placement, fixing method, and external forces. Typically, we use the Fixed Constraint node to ensure zero displacement:

$$\boldsymbol{u} = \mathbf{0} \tag{23}$$

in all directions on the selected geometrical entities, effectively fixing the device. For other non-fixed surfaces, Free nodes, Boundary Load, and other boundary conditions are applied based on the actual scenario.

D. Coupling Relationships in EM-Thermal-Mechanical Multiphysics for Sensor System

Here, we synthesize the governing equations of the three physical fields and their pairwise couplings, summarized as follows.

- **EM-thermal coupling**
  EM → thermal: the dissipated power of the electromagnetic field (i.e., microwave heating in wireless sensor) is introduced as a heat source term Q_{em} in the thermal conduction equation.
  Thermal → EM: temperature variations induce changes in the substrate permittivity $\varepsilon(T)$, leading to shifts in the sensor's resonant frequencies.
- **EM-mechanical coupling**
  EM → mechanical: application of an electric field induces stress and strain in the piezoelectric material via the inverse piezoelectric effect (i.e., electrostriction);
  Mechanical → EM: for piezoelectric materials, mechanical stress generates electric charge through the direct piezoelectric effect; in addition, pressure-dependent permittivity $\varepsilon(P)$ and structural deformations alter the EM response.
- **Thermal-mechanical coupling:**
  Thermal → mechanical: temperature changes produce thermal stress and strain (i.e., thermal expansion or contraction).
  Mechanical → thermal: structural deformations intrinsically modify the spatial temperature distribution $T(\boldsymbol{r})$, which reflects the altered geometry.

To quantitatively evaluate the coupling effects, the governing equations and corresponding boundary conditions of the interacting fields should be applied. For clarity, the field governing equations and the corresponding coupling principles are summarized in Fig. 1. In theory, each pair of coupled fields involves two one-way interactions that mutually influence each other and evolve simultaneously. However, the characteristics of the simulation problem must be further analyzed to determine whether these one-way interactions can be computed independently or require iterative treatment.

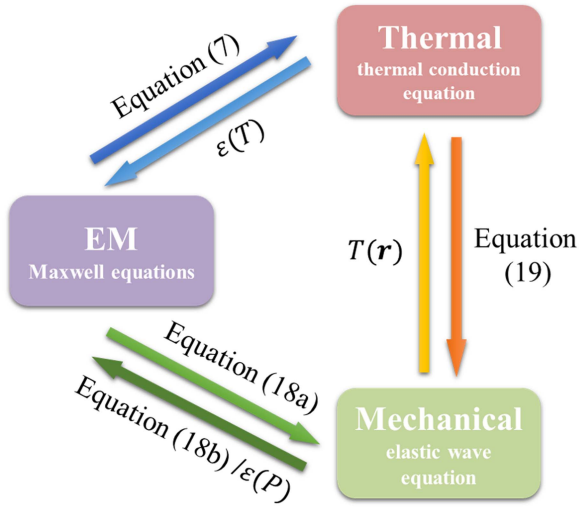

Fig. 1. Coupling mechanics and equations of EM-thermal-mechanical multiphysics model for sensor systems.

III. Simulation of Temperature Sensor

A specific resonator is used as an example of a temperature sensor to demonstrate the quantitative evaluation of coupling effects in the multiphysics model of a wireless passive sensor. The simulation is conducted based on the EM-thermal-mechanical multiphysics model, enabling the temperature monitoring mechanisms to be clarified and validated from a multiphysics perspective. Sections III-B, III-C, and III-D present the simulation and analysis of the different types of coupling effects for this sensor model.

A. Design of Resonator for Temperature Monitoring

Spiral resonator structures, known for their simple geometry and high-Q resonance, have been widely used in metamaterial-based sensing applications [39], [40], [41], [42]. In this section, such structures are employed to demonstrate the proposed multiphysics simulation framework for analyzing coupled EM-mechanical-thermal effects. The variation in the dielectric constant of the ceramic substrate leads to a shift in the resonant frequency of the resonator, which serves as the fundamental principle for temperature monitoring.

The unit cell of a 16-branch spiral resonator for temperature monitoring is shown in Fig. 2. The resonator consists of a metallic resonant structure (perfect electric conductor, PEC), a dielectric substrate, and a metal ground (GND) plane, forming a sandwich-like configuration. The substrate dimensions are

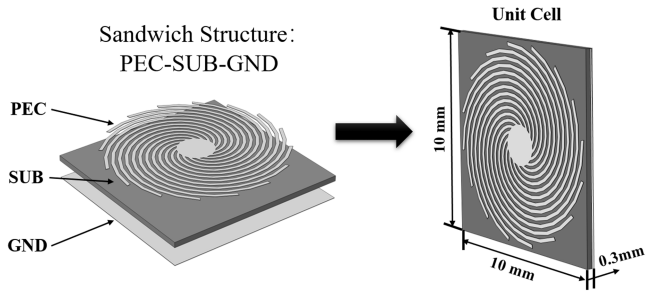

Fig. 2. The structure diagram of the 16-branch spiral resonator.

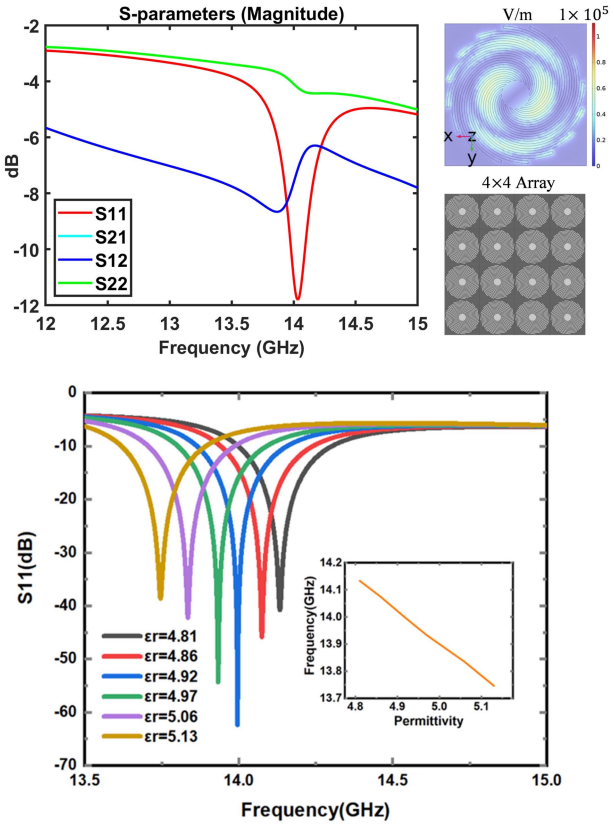

Fig. 3. S-parameter curves of the spiral resonator for the unit cell and 4× 4 array structures.

set to 10 mm × 10 mm × 3 mm to achieve a working frequency range of 12–15 GHz. Aluminum oxide (Al_2O_3), with a temperature-dependent dielectric constant, is selected as the substrate material, while platinum (Pt), known for its high-temperature stability, is used as the PEC to enable temperature sensing. This structure is classified as a scattering-absorption integrated metamaterial sensor, where the ground plane reflects electromagnetic waves absorbed by the resonator at a specific resonant frequency.

The upper part of Fig. 3 shows the S-parameter curves of the unit cell, where the S_{12} and S_{21} curves coincide. The lower part of Fig. 3 presents the resonant response of the 4× 4 array, illustrating the frequency shift caused by variations in the substrate dielectric constant. The inset shows that the resonant frequency varies approximately linearly with the dielectric constant. The upper-right insets of Fig. 3 depict the 4×4 array structure and the electric field distribution of the unit cell at resonance.

TABLE I
THE PARAMETERS OF MATERIALS IN SIMULATIONS

	EM parameters		Thermal parameters		
	ε	$tan\delta$	k^1	C_p^2	ρ^3
SUB	4.81	0.0185	35	730	3750
PEC		\	71.6	133	21500

1. Thermal Conductivity [W/(m · K)]
2. Specific Heat Capacity at Constant Pressure [J/(kg · K)]
3. Density [kg/m^3]

COMSOL Multiphysics is employed to investigate the multiphysics coupling effects in the temperature sensor model. Simulations are performed on the unit cell to capture the essential coupling mechanisms. Thermal boundary conditions include a fixed temperature at the bottom and convective conditions on the outer surfaces, while mechanical boundary conditions consist of a fixed constraint at the bottom and a pressure load on the top surface. A physics-controlled mesh with regular free tetrahedral elements is used for all models.

B. EM-Thermal Coupling Effect

The **EM → thermal** coupling is modeled by incorporating the microwave heat source generated from EM power dissipation (7) into the heat conduction equation (6) as a volumetric source. The temperature distribution is solved using the **Microwave Heating interface** in COMSOL Multiphysics, which couples the **RF Module** and the **Heat Transfer Module**.

In this sensor model, platinum (Pt) is adopted as the PEC material, and aluminum oxide (Al2O3) serves as the substrate. For Heat Transfer Module setting, the bottom temperature is set to $To = 300$ K, the convective heat transfer coefficient to $h = 15$ W/(m^2 · K), and the ambient air temperature to $Tsur = 293.15$ K. To enhance the EM-thermal coupling effect, the incident electromagnetic wave is excited through a rectangular port, with the frequency tuned near the device's resonance (14 GHz). Under this condition, the resulting power dissipation (computed through the Microwave Heating interface) generates a more pronounced microwave heat source for the subsequent thermal analysis. The material parameters employed in the simulations are summarized in Table I.

To evaluate the influence of microwave heating on the sensor's thermal behavior, Fig. 4 presents the simulated surface temperature distributions of the substrate and spiral metal patch under conditions with and without the microwave heat source. When the microwave heat source is introduced, the localized enhancement of the electric field intensity (as shown in the upper right illustration of Fig. 3) corresponds to a slightly nonuniform temperature distribution (with a maximum temperature difference below 0.012 K) exhibiting central symmetry consistent with the device geometry, as illustrated in Fig. 4(b). This correspondence confirms the effective incorporation of the *EM → mechanical* coupling in the simulation.

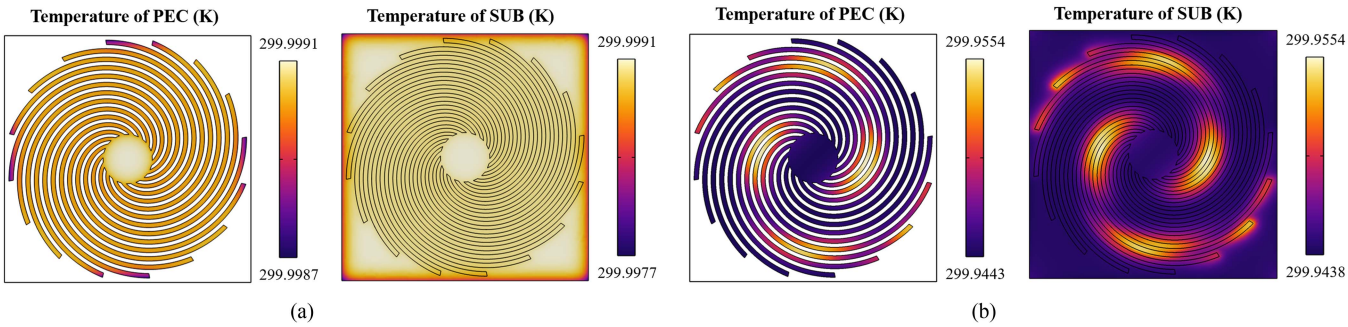

Fig. 4. Temperature distribution of the sensor device. (a) Without microwave heat source (i.e., no coupling). (b) With microwave heat source (i.e., coupling).

TABLE II
AVERAGE TEMPERATURE AND MAXIMUM TEMPERATURE DIFFERENCE OF THE UPPER SURFACE OF THE SUBSTRATE UNDER DIFFERENT BOTTOM FIXED TEMPERATURE AND DIFFERENT HEAT SOURCE CONDITIONS

Bottom temperature (K)		500	600	700	800	900	1000
Average temperature (K)	Without EM heating	499.94	599.91	699.87	799.83	899.78	999.72
	With EM heating	499.93	599.89	699.85	799.80	899.75	999.72
Maximum temperature difference (K)	Without EM heating	0.07	0.12	0.17	0.22	0.28	0.36
	With EM heating	0.1	0.14	0.17	0.23	0.28	0.35

To quantitatively evaluate the effect of microwave heating, the average temperature and maximum temperature difference of the substrate's upper surface were computed under various bottom surface temperatures, as summarized in Table II. The results show that the inclusion of the electromagnetic heat source slightly alters the heat distribution but induces only a negligible temperature rise ($\sim 10^{-2}$ K) compared with the overall temperature range (10^2–10^3 K), indicating that its thermal impact is insignificant.

An additional investigation was conducted to assess the influence of the external air environment on the sensor temperature. Two ambient temperatures, 293.15 K and 1000 K, representing typical and high-temperature conditions, were considered, with the heat transfer coefficient varied from 25 to 250 $\mathrm{W}/(\mathrm{m}^2 \cdot \mathrm{K})$. The results show that both the average and maximum temperatures change by less than 1 K, indicating that the sensor temperature is largely insensitive to variations in ambient conditions and heat transfer coefficient, and is primarily determined by heat transfer from the underlying object.

To investigate the **thermal**→ **EM** coupling, two simulations were conducted to assess the effect of non-uniform internal temperature on the device's electromagnetic response. In the first, a pure EM simulation assumed a uniform temperature, with constant dielectric parameters (e.g., permittivity at 500 K) and no heat transfer. In the second, an EM-thermal multiphysics simulation accounted for the non-uniform temperature distribution within the substrate, with permittivity and loss tangent defined as temperature-dependent functions, $\varepsilon_r(T)$ and $\tan\delta(T)$ (left inset of Fig. 5). EM models used rectangular ports for excitation, while heat conduction and EM boundary conditions followed those in Fig. 4. Temperature differences were introduced via EM heat sources, causing local variations in dielectric parameters. The results, shown in Fig. 5, illustrate the impact of thermal non-uniformity on resonance.

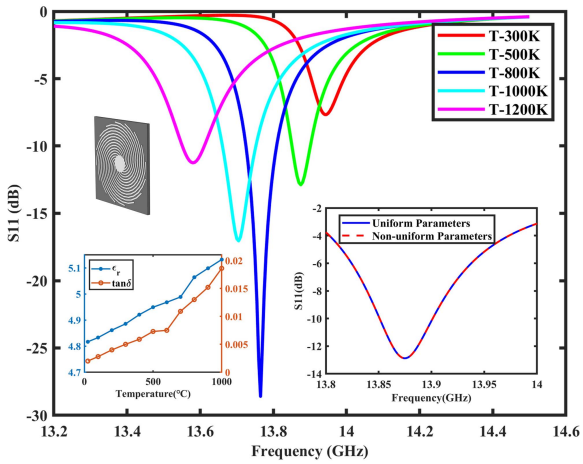

Fig. 5. EM simulation versus EM-thermal simulation: a comparison of S_{11} curves.

According to the inset on the right of Fig. 5, no significant shift is observed in the curves. Numerical results indicate that the difference in S_{11} parameters obtained from the two simulation methods at the same frequency is on the order of 10^{-3} dB, which can be neglected. This negligible effect is attributed to the relatively small temperature differences generated by electromagnetic heating within the device compared to the high-temperature ambient conditions.

The primary EM-thermal coupling effect is observed in the shift of the S_{11} curve caused by changes in the device bottom temperature. The sensor's EM response spectrum is mainly governed by the temperature-dependent permittivity of the substrate, where the dielectric constant increases with temperature [43]. In COMSOL, the EM parameters are set as interpolation functions of temperature, and EM-thermal

simulations are performed on a unit of the spiral resonator at different temperatures. As shown in Fig. 5, both the real part of the dielectric constant ε_r and the loss tangent $\tan\delta$ of the ceramic material increase with temperature, resulting in the observed shift of the S_{11} resonance.

An increase in the substrate dielectric constant enhances its polarization, analogous to increasing the capacitance in an LC resonant circuit, which lowers the resonant frequency and shifts the resonance curve to the left. Simultaneous changes in dielectric loss modulate this effect: moderate loss increases EM wave absorption, deepening the S_{11} resonance, while excessive loss raises the overall dissipation, reducing the Q factor and shallowing the peak. Dielectric loss can thus be regarded as the equivalent resistance in an RLC circuit, with optimal resonance achieved when the material exhibits slight loss, near the impedance-matching condition. Consequently, in Fig. 5, the resonance peak is deepest and sharpest when the dielectric loss takes an intermediate value, whereas peaks corresponding to lower or higher loss are shallower and broader, consistent with the above analysis.

C. EM-Mechanical Coupling Effect

The EM–mechanical coupling effect can be categorized into two aspects: the structural stress and strain induced by electromagnetic fields, and the EM response variations caused by structural deformation and/or pressure-dependent dielectric properties of the material. The mechanical behavior related to this coupling is analyzed using the **Structural Mechanics Module** in COMSOL Multiphysics.

The **EM** $\rightarrow$ **mechanical** coupling is negligible in passive microwave sensors, as the internal field is a high-frequency resonant electromagnetic field rather than a static electric field, which does not induce appreciable electrostrictive or inverse piezoelectric effects. Consequently, the device structure remains essentially unaffected by incident EM waves. For active device applications where electrostatic-mechanical interactions are relevant, such coupling can be analyzed using the Piezoelectricity Interface in COMSOL Multiphysics.

The **mechanical** $\rightarrow$ **EM** coupling can arise from two factors: (1) structural deformation under external pressure, and (2) pressure-dependent variations in the dielectric properties of the substrate. The latter is not relevant to temperature sensing applications, as the materials employed are typically insensitive to pressure, thereby avoiding unintended EM-mechanical coupling.

The sensor is designed to operate in extreme environments with high temperature and pressure, capable of withstanding external loads up to 1–5 MPa. A uniform external pressure is applied to the top surface (**Boundary Load**), while the bottom surface is fixed to represent the mechanical constraints (**Fixed Constraint**). The material properties, including Young's modulus (PEC: 1.68×10^{11} Pa; SUB: 7.48×10^{11} Pa) and Poisson's ratio (PEC: 0.38; SUB: 0.45), are specified as input parameters. The resulting stress and strain distributions are obtained by solving the steady-state elastic equation, with the applied pressure varied from 1 MPa to 5 MPa during the simulation.

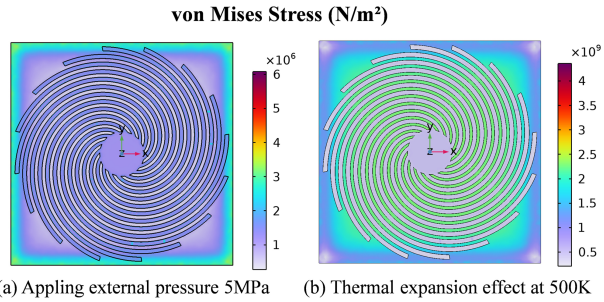

(a) Appling external pressure 5MPa (b) Thermal expansion effect at 500K

Fig. 6. Schematic diagram of stress distribution on the surface of the structure under the effect of external pressure and thermal expansion.

TABLE III
STRUCTURAL STRESS AND STRAIN UNDER DIFFERENT PRESSURE

Pressure (Pa)	von Mises Stress (N/m^2)	Volumetric Strain
1.0×10^6	3.8939×10^5	-3.1732×10^{-6}
2.0×10^6	7.7879×10^5	-6.3463×10^{-6}
3.0×10^6	1.1682×10^6	-9.5195×10^{-6}
4.0×10^6	1.5576×10^6	-1.2693×10^{-5}
5.0×10^6	1.9470×10^6	-1.5866×10^{-5}

Fig. 6(a) illustrates the three-dimensional stress distribution on the device surface. Table III summarizes the von Mises stress (a scalar equivalent stress derived from the Cauchy stress tensor, commonly used to predict yielding under complex loading) and the volumetric strain (the relative volume change under uniform stress) at the center of the upper substrate surface. As the applied pressure on the upper surface increases, both internal stress and strain rise correspondingly, with negative strain values indicating volumetric compression. However, the strain magnitude ($\sim 10^{-6}$–10^{-5}) suggests that the structural deformation is negligible. Therefore, for thin-layer microwave sensors such as spiral resonators, the influence of pressure-induced deformation on the EM response spectrum can be reasonably neglected. In contrast, for deformable resonant structures (such as those incorporating a sealed cavity with a flexible diaphragm) the EM-mechanical coupling becomes significant, which will be further analyzed in the subsequent section on pressure sensors.

D. Thermal-Mechanical Coupling Effect

To quantify the effect of *thermal* $\rightarrow$ *mechanical* coupling, the influence of material thermal expansion is primarily considered. The simulations are conducted using the **Heat Transfer Module** and **Structural Mechanics Module**, with the **Thermal Expansion** multiphysics coupling in COMSOL employed to capture the interaction between temperature variation and structural deformation.

In this analysis, the ambient temperature is set to 293.15 K, and the coefficients of thermal expansion are specified as 8.8×10^{-6} K^{-1} for the PEC and 8×10^{-6} K^{-1} for the silicon carbide (SiC) substrate. It should be noted that the thermal expansion coefficient may vary with temperature; however, it is treated as constant here for simplicity and analytical clarity.

The von Mises stress distribution of the structure at 500 K is shown in Fig. 6(b), which illustrates the magnitude of internal

TABLE IV
STRUCTURAL STRESS AND STRAIN UNDER DIFFERENT TEMPERATURE

Temperature (K)	von Mises Stress (N/m^2)	Volumetric Strain
500	4.8209×10^{8}	4.0535×10^{-3}
600	7.2998×10^{8}	6.0130×10^{-3}
700	9.6786×10^{8}	7.9725×10^{-3}
800	1.2057×10^{9}	9.9319×10^{-3}
900	1.4436×10^{9}	1.1891×10^{-2}

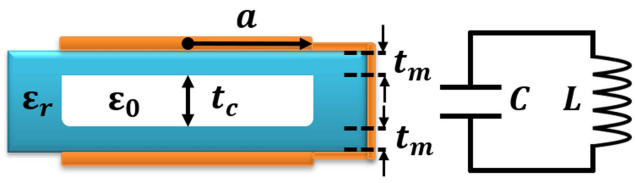

Fig. 7. Schematic Cross Section and Equivalent Circuit of LC Resonator.

stress induced by thermal expansion at elevated temperatures. Table IV presents the numerical results of stress and strain under thermal expansion at different device temperatures, indicating that both quantities increase with temperature. In the high-temperature range of 500 K–1000 K, the structural thermal strain is on the order of 10^{-3}–10^{-2}, which is significantly larger than the compression strain induced by external pressure, yet still negligible relative to the overall structural dimensions. Therefore, for the spiral resonator configuration, the thermal expansion effect (*thermal* $\rightarrow$ *mechanical* coupling) does not notably alter the electromagnetic response of the device. Notably, in multiphysics coupling scenarios relevant to high-temperature and high-pressure environments, the thermal expansion effect exerts a more significant influence than the pressure-induced compression effect.

For the **mechanical** $\rightarrow$ **thermal** coupling, since the structural deformation of the device remains negligible under high-temperature and high-pressure multiphysics conditions, its influence on the thermal field can be ignored. To perform this type of coupling, it is sufficient to conduct a thermal simulation in COMSOL on the mesh of the Deformed Geometry interface with the applied pressure load.

In summary, the multiphysics analysis of the spiral-structured temperature sensor demonstrates that variations in the material's dielectric properties (induced by environmental factors such as temperature and pressure) are the primary causes of shifts in the electromagnetic response spectrum. Other coupling effects, including microwave heating and thermal expansion, have negligible impact and can be omitted in the simulation of such metamaterial microwave sensors.

IV. SIMULATIONS OF PRESSURE SENSOR

The multiphysics modeling of wireless passive pressure sensors follows the same simulation framework established for the temperature sensor in Section III. In contrast, the analysis here focuses on resonant structures with deformable cavities, where structural deformation and pressure-dependent permittivity jointly influence the electromagnetic response. Accordingly, the coupling analysis emphasizes the EM-mechanical and thermal-mechanical interactions, while the boundary conditions and meshing strategy remain consistent with those used in the temperature sensor model.

A. Working Principle and Design of Pressure Sensor With Deformable Structure

Wireless passive pressure sensors typically employ a sealed cavity and deformable materials to enable elastic deformation under external pressure. For some bulk-structure sensors, pressure sensing relies on the piezo-dielectric properties of the substrate, analogous to the temperature sensing mechanism in passive temperature sensors. In this subsection, the focus is on pressure sensing based on a deformable cavity.

Resonators containing cavities operate according to two main principles. One is based on standing-wave physics, involving half-wavelength resonance between the electromagnetic field and the cavity. The other is based on the equivalent circuit model, where resonance is determined by the device's effective inductance and capacitance.

For **cavity resonance mechanism**, the sensitivity of a microwave sensor can be analyzed using cavity perturbation theory. For a deformable cavity, the resonant frequency variation due to a small shape perturbation can be approximated as

$$\frac{\omega-\omega_0}{\omega_0}\approx\frac{\iiint_{\Delta V}\left(\mu\left|\mathbf{H_0}\right|^2-\varepsilon\left|\mathbf{E_0}\right|^2\right)dv}{\iiint_{V}\left(\mu\left|\mathbf{H_0}\right|^2+\varepsilon\left|\mathbf{E_0}\right|^2\right)dv} \tag{24}$$

or

$$\frac{\omega-\omega_0}{\omega_0}\approx\frac{\Delta W_m-\Delta W_e}{W_m+W_e} \tag{25}$$

where ΔW_m and ΔW_e represent time-average magnetic and electric energies in the perturbed volume ΔV. Since $\Delta V \ll V$, $\Delta W \approx \frac{\Delta V}{V} W$, indicating that the shift of resonant frequency $\Delta f/f \propto \Delta V/V$. For a cylindrical cavity with radius a and height t_c as an example, $\Delta f/f \propto \Delta t/t_c$ where Δt is the height displacement due to external pressure. Since the displacement of the cavity height is generally proportional to the external pressure applied to the device [26], i.e., $\Delta f/f \propto \Delta P$. Therefore, the pressure sensitivity $\Delta f/\Delta P$ can be expressed as a positive coefficient that related to deformation properties of the cavity and the design of resonator, i.e., $P\uparrow \Rightarrow f_{reso}\uparrow$.

For **LC equivalent circuit mechanism**, the sensitivity of a LC resonator sensor according to deformable structure can be analyzed based on the equation of LC resonance's equivalent frequency $f = 1/2\pi\sqrt{LC}$. As illustrated in Fig. 7 (orange color represents metal material and the blue color represents substrate dielectric material), the parallel capacitance of a cavity-containing resonator can be approximated as

$$C_0 = \frac{\varepsilon_0 \pi a^2}{t_c + 2t_m\varepsilon_r^{-1}}. \tag{26}$$

When external pressure compresses the cavity, the cavity height decreases ($t_c\downarrow$), increasing the equivalent capacitance ($C_0\uparrow$). And the resonant frequency decreases as the equivalent capacitance increases, i.e., $\Delta f = f - f_0 \propto -1/\sqrt{\Delta C} \propto -\sqrt{\Delta t}$

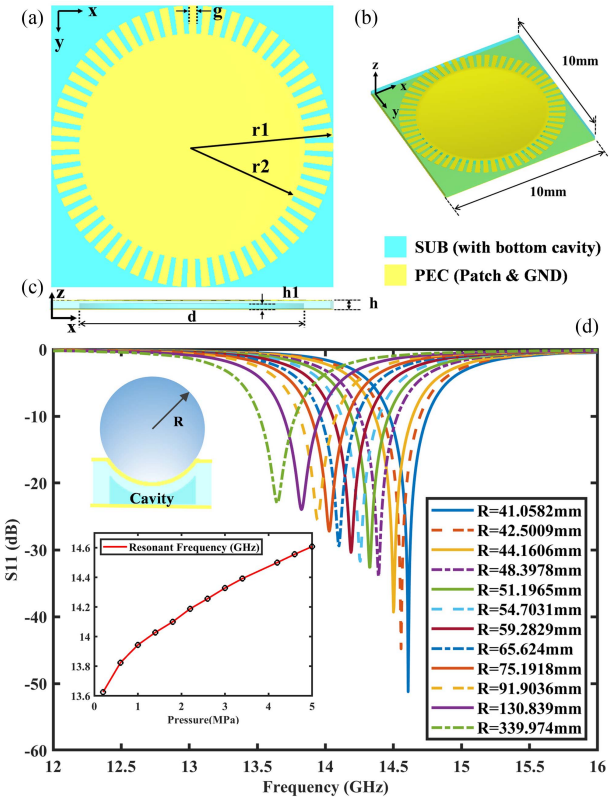

Fig. 8. Schematic diagram and resonant curve of a multi-slot structural pressure sensor.

($\Delta f < 0$). Therefore, the sensitivity of an LC resonator, implemented as a pressure sensor through a deformable cavity, can be quantified by a negative coefficient, i.e., $P \uparrow \Rightarrow f_{reso} \downarrow$. The magnitude of the sensitivity depends on the cavity's mechanical properties and the resonator design.

Based on the resonant cavity principle, a multi-slot resonator is designed, consisting of a multi-slot metal patch (PEC), a 10 mm × 10 mm × 0.3 mm substrate with a sealed bottom cavity (radius 4 mm, height 0.2 mm), and a metal ground plane (GND), as shown in Fig. 8. To model the cavity deformation under external pressure, a concave spherical crown (inset of Fig. 8(d)) is applied to the upper surface using the Bend Shape function in CST Studio Suite, with curvature determined from the maximum displacement obtained in mechanical simulations. The resulting structural deformation shifts the resonant frequency upward as pressure increases (0.2–5 MPa), as indicated by the S_{11} curves.

For the LC equivalent circuit resonance principle, a PEC-GND connected model with a 11 mm × 11 mm × 1 mm substrate which contains a cavity of 5.2 mm radius and 0.05 mm heightis designed, as shown in Fig. 9. By changing the thickness of the middle cavity, the resonant frequency shifts effectively (the results will be shown in the following section), which is significant for pressure sensing.

The sensitivity of the pressure sensor, designed according to these two principles, is primarily dependent on the structural design and the material's deformation characteristics. However, the pressure response frequency shifts in opposite directions for the two pressure-sensing working principles.

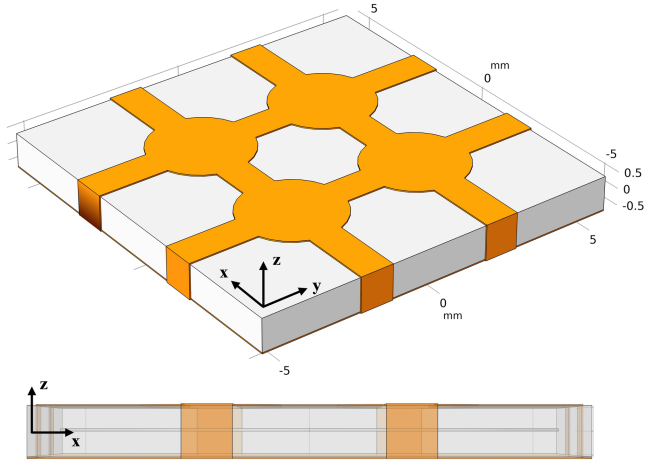

Fig. 9. Schematic diagram of a equivalent LC resonator sensor.

For the LC equivalent circuit principle, a PEC–GND model (comprising a PEC patch, a ground plane, and sidewall metal strips connecting the patch and ground plane) is employed, featuring an 11 mm × 11 mm × 1 mm substrate with a cavity (radius 5.2 mm, height 0.05 mm) (Fig. 9). Variation of the cavity thickness effectively shifts the resonant frequency, providing the basis for pressure sensing. Based on this design, the multiphysics effects of the pressure sensor are further investigated using the **same COMSOL modules** employed for the temperature sensor simulations in Section III; the similar simulation settings will not be reiterated.

B. EM-Mechanical Coupling Effect

Since the excitation is an electromagnetic wave applied through a rectangular port and the materials in the microwave sensor system are non-piezoelectric, the inverse piezoelectric effect (i.e., the *EM* → *mechanical* coupling) is neglected. Consequently, the analysis focuses on the *mechanical* → *EM* coupling effect, i.e., the influence of structural deformation on the electromagnetic response.

Structural deformation of the pressure sensor under applied pressure is first simulated in COMSOL Multiphysics using a physics-controlled mesh, where the element size is adjusted to ensure convergence of the mechanical displacement results while balancing accuracy and computational efficiency. Conventional analyses of cavity-based pressure sensors often rely on simplified substrate models; however, neglecting the distinct mechanical characteristics of metallic components may lead to deviations in the predicted deformation. Therefore, a full sensor model is implemented in COMSOL to perform a more detailed mechanical simulation and validate the multiphysics coupling effects.

Mechanical simulations were conducted with the lower surface fixed and a uniform pressure applied to the upper surface, for both a simplified substrate-only model and a complete device model incorporating the PEC layer. The resulting stress distributions on the substrate and PEC surfaces are presented in Fig. 10, while the corresponding deformation results are

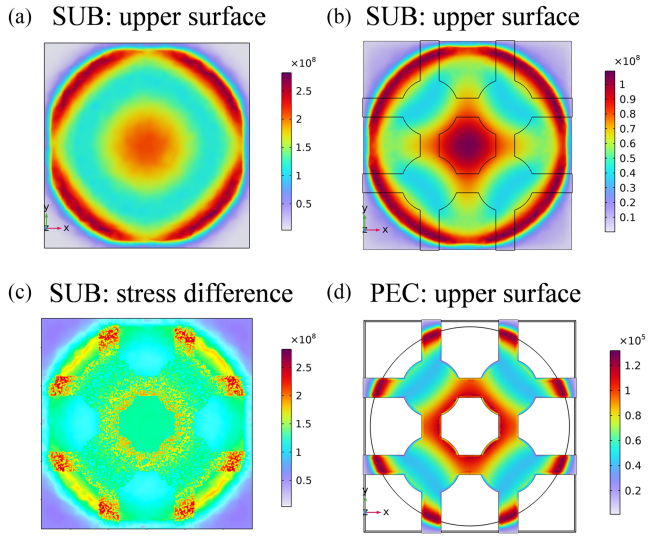

Fig. 10. Von Mises stress distribution of the sensor device: comparison between the simplified substrate model and the complete structure. (a) Stress distribution on the upper surface of the substrate in the simplified model. (b) Stress distribution on the upper surface of the substrate in the complete model. (c) Difference plot showing the result of (a) minus (b). (d) Stress distribution on the upper surface of the PEC patch.

TABLE V
CENTER POINT DEFORMATION AND AVERAGE DEFORMATION OF UPPER SURFACE OF THE CAVITY UNDER DIFFERENT CONDITIONS

	Center point deformation (mm)		Average deformation (mm)	
	Without PEC patch	With PEC patch	Without PEC patch	With PEC patch
Without thermal expansion	-0.048096	-0.022618	-0.018304	-0.0089944
With thermal expansion	-0.042215	-0.018807	-0.014220	-0.0068970

Notes: the applied pressure is 3 MPa; set the temperature to 500 K for thermal expansion effect.

TABLE VI
COMPARISON OF THE PROPOSED MODELS TO PREVIOUS MODELS

Reference	Accuracy of Resonant Frequency	Accuracy of S11 Parameters	Simulation Models
[29]	+5.5%, -5.2%	/	deflection theory
[30]	2.46%	/	deflection theory
[31]	38.2%, 44.3%	/	deflection simulation
[32]	1-12.5%	/	deflection theory
This work (Simple Model)	2.65%	101.92%	EM & Mechanical simulation
This work (Bend Shape Model)	0.32%	13.15%	EM & Mechanical simulation

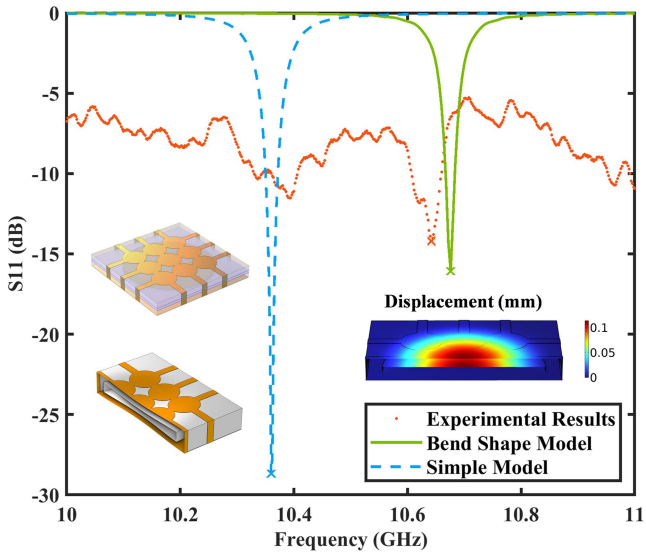

Fig. 11. Comparison of simulation and experimental results of S_{11} curve of LC resonator sensor.

summarized in Table V under the without thermal expansion condition. As illustrated in Fig. 10, the maximum stress on the substrate surface in the complete model is markedly lower than that in the simplified model, while the stress within the PEC layer remains relatively small. This demonstrates that the metal layer effectively redistributes structural stress and mitigates deformation within the dielectric substrate. The deformation data further indicate that the displacement difference between the models with and without the PEC patch is considerable, with the simplified model exhibiting up to 112% higher deformation. Such discrepancy underscores the inaccuracy of simplified models and the necessity of employing the complete structural model to ensure reliable coupling analysis.

Mechanical simulation results indicate that the upper surface of the cavity exhibits a dome-shaped deformation (inset of Fig. 11), with the maximum displacement at the center gradually decreasing toward the edges, which can be effectively approximated by a spherical crown. The central displacement extracted from the mechanical simulation under different external pressure is subsequently coupled into the EM model using the Bend Shape function to realize the **mechanical** $\rightarrow$ **EM** coupling.

To validate the effectiveness of the mechanically coupled EM model, the proposed precise modeling approach is compared with a simpler non-coupled simulation method using experimental measurements as the reference (Fig. 11). For experimental validation, the LC resonator sensor (similar to the structure in Fig. 9, with more complex patch patterns shown in the insets of Fig. 11) was mounted on a customized fixture inside a sealed pressure chamber. The interrogation antenna was connected to an Agilent E5063 A vector network analyzer (VNA) via a 50-Ω coaxial cable to record the measurements. All data presented were independently obtained, while the experimental setup followed a configuration similar to prior work (Wang et al., arXiv:2411.16759). A single 1.5MPa pressure-loading experiment (red dots in Fig. 11) is used in this study to directly compare experimental results with simulation predictions. At non-resonant frequencies, the experimentally measured $|S_{11}|$

TABLE VII
CENTER POINT DEFORMATION AND AVERAGE DEFORMATION OF DEVICE UNDER DIFFERENT TEMPERATURE CONDITIONS

	Mechanical simulation	Mechanical-thermal coupling simulation (300K)	Mechanical-thermal coupling simulation (500K)	Mechanical-thermal coupling simulation (800K)
Cavity upper surface: average displacement (mm)	-0.0089944	-0.0089058	-0.0068970	-0.0058852
Cavity upper surface: center point displacement (mm)	-0.022618	-0.022480	-0.018807	-0.014054
SUB upper surface: center point displacement (mm)	-0.022617	-0.022454	-0.018056	-0.012227
SUB upper surface: center point von Mises Stress (Pa)	1.0654E8	1.0670E8	1.0791E8	9.2696E7

magnitude is higher than the near-zero simulation values, primarily due to parasitic effects, impedance mismatch, environmental noise, and intrinsic device losses.

A simple modeling approach adjusts only the substrate and cavity heights, whereas the proposed bend shape model more accurately captures the sensor's deformation. EM simulations using these two methods, combined with mechanical simulations, are shown in Fig. 11 (green and cyan lines, respectively). The bend shape model shows closer agreement with experimental results in both resonant frequency and S_{11} dip depth, achieving a frequency accuracy of 0.32% versus 2.65% for the simple model, and an S_{11} accuracy of 13.15% versus 101.92%. These results demonstrate the improved accuracy of the EM-mechanical coupling approach. Compared with literature models (Table VI), the bend shape model achieves significantly higher accuracy in resonant frequency prediction. Unlike most prior approaches, which rely on analytical deflection theory or simple mechanical simulations, our model incorporates detailed EM-mechanical coupling and can accommodate complex device geometries and multiple materials, demonstrating its advantages despite increased modeling complexity.

C. Thermal-Mechanical Coupling Effect

For high-temperature applications, thermal expansion must be carefully considered in multi-physics simulations to accurately capture the **thermal** $\rightarrow$ **mechanical** coupling in pressure sensors.

The deformation results at 500 K, presented in the with thermal expansion condition of Table V, are compared with ambient temperature conditions (i.e., without thermal expansion), indicating that including thermal expansion reduces the cavity deformation by approximately 10–25%. Furthermore, Table VII summarizes the deformation under multiple temperature conditions, showing that the influence of thermal expansion becomes more pronounced as temperature increases, further reducing the cavity deformation.

By incorporating these mechanical simulation results that account for thermal expansion into the electromagnetic model, a comprehensive EM-mechanical-thermal multiphysics sensor model is established. This integrated model enables accurate pressure monitoring under combined high-temperature and high-pressure conditions, reflecting the coupled effects of electromagnetic, mechanical, and thermal fields.

Although the COMSOL Multiphysics models (based on the finite element method, FEM) effectively capture the multiphysics behavior of the pressure sensor, their accuracy remains constrained by numerical and modeling assumptions. Mesh resolution can affect stress localization, while idealized material and boundary conditions may deviate from experimental realities. Hence, the simulation results should be interpreted with caution and validated against measurements.

Despite these limitations, the established FEM framework provides a reliable foundation for analyzing EM–thermal–mechanical coupling effects. The results confirm that structural deformation and thermal expansion are the dominant factors influencing the EM response of deformable pressure sensors, offering clear guidance for model simplification and performance optimization.

Data Availability: The COMSOL Multiphysics simulation files associated with this study are provided at [44].

V. CONCLUSION

This study presented a comprehensive investigation of EM-thermal-mechanical coupling in wireless passive microwave sensors and established a unified multiphysics modeling framework applicable to both temperature and pressure sensing. The framework integrates governing equations of the three physical fields, defines boundary conditions through bidirectional and unidirectional coupling pathways, and quantitatively evaluates their relative significance by numerical simulations.

Systematic simulations revealed that dielectric property variations induced by temperature are the primary factors influencing the EM response of microwave sensors, while secondary effects such as microwave heating and structural thermal expansion can be reasonably simplified for the spiral-type thin-film resonators. In contrast, for deformable cavity-based pressure sensors, incorporating structural deformation and thermal expansion markedly improves predictive accuracy.

This work underscores the importance of considering multiphysics coupling in sensor modeling to improve design reliability and provides practical guidance on balancing model complexity and computational efficiency. Future research will focus on optimizing mesh strategies, adopting more realistic material models, and refining boundary representations to further enhance accuracy. In addition, the framework can be extended to include electromechanical or electrostatic coupling (e.g., piezoelectric effects) and circuit-level co-simulation, enabling the modeling of more diverse material systems and next-generation wireless passive sensors with greater functional integration.

REFERENCES

[1] T. George, K. Son, R. Powers, L. Del Castillo, and R. Okojie, "Harsh environment microtechnologies for NASA and terrestrial applications," in *Proc. IEEE Sensors*, Irvine, CA, USA, 2005, pp. 1253–1258.

[2] R. W. Johnson, J. L. Evans, P. Jacobsen, J. R. Thompson, and M. Christopher, "The changing automotive environment: High-temperature electronics," *IEEE Trans. Electron. Packag. Manuf.*, vol. 27, no. 3, pp. 164–176, Jul. 2004.

[3] W. C. Wilson and G. M. Atkinson, "Passive wireless sensor applications for NASA's extreme aeronautical environments," *IEEE Sensors J.*, vol. 14, no. 11, pp. 3745–3753, Nov. 2014.

[4] M. P. Boyce, *Gas Turbine Engineering Handbook*. New York, NY, USA: Elsevier, 2011.

[5] J. Daniel, S. Nguyen, M. A. R. Chowdhury, S. Xu, and C. Xu, "Temperature and pressure wireless ceramic sensor (distance= 0.5 meter) for extreme environment applications," *Sensors*, vol. 21, no. 19, 2021, Art. no. 6648.

[6] R. S. Okojie, A. A. Ned, and A. D. Kurtz, "Operation of α(6H)-SiC pressure sensor at 500°," *Sensors Actuator A-Phys.*, vol. 66, no. 1, pp. 200–204., 1998.

[7] N. R. Kumar et al., "Crystallization and creep behavior of SI–B–C–N ceramics," *Acta Mater.*, vol. 53, no. 17, pp. 4567–4578, 2005.

[8] Y. Wang, W. Fei, Y. Fan, L. Zhang, W. Zhang, and L. An, "Silicoaluminum carbonitride ceramic resist to oxidation/corrosion in water vapor," *J. Mater. Res.*, vol. 21, no. 7, pp. 1625–1628, 2006.

[9] X. Ren, S. Ebadi, Y. Chen, L. An, and X. Gong, "Characterization of SiCN ceramic material dielectric properties at high temperatures for harsh environment sensing applications," *IEEE Trans. Microw. Theory Tech.*, vol. 61, no. 2, pp. 960–971, Feb. 2012.

[10] D. Gibbs and G. Hill, "The variation of the dielectric constant of diamond with pressure," *Philos. Mag.*, vol. 9, no. 99, pp. 367–375, 1964.

[11] C. Tan, B. Li, Y. Liu, W. Ge, and B. Sun, "Multiphysics methodology for thermal modelling and quantitative analysis of electromagnetic linear actuator," *Smart Mater. Struct.*, vol. 28, no. 8, 2019, Art. no. 087001.

[12] J. M. Jin and S. Yan, "Multiphysics modeling in electromagnetics: Technical challenges and potential solutions," *IEEE Antennas Propag. Mag.*, vol. 61, no. 2, pp. 14–26, Apr. 2019.

[13] X. Chen, L. Wang, D. Pommerenke, and M. Yu, "Passive intermodulation on coaxial connector under electro-thermal-mechanical multiphysics," *IEEE Trans. Microw. Theory Tech.*, vol. 70, no. 1, pp. 169–177, Jan. 2022.

[14] H. H. Zhang et al., "Electromagnetic-circuital-thermal-mechanical multiphysics numerical simulation method for microwave circuits," *IEEE J. Multiscale Multiphys. Comput. Technol.*, vol. 9, pp. 129–141., 2024.

[15] H. H. Zhang, X. Y. Liu, Y. Liu, Z. C. Fan, and H. L. Du, "Thermal-mechanical-electromagnetic multiphysics simulation of satellite phased array antenna based on DGTD and FEM method," *IEEE J. Multiscale Multiphys. Comput. Technol.*, vol. 9, pp. 236–246., 2024.

[16] W. Wei, X. Chen, Z. Zong, R. Qiao, Z. Shao, and N. Ni, "Study on the electromagnetic-thermal-mechanical coupling damage of concrete under microwave irradiation," *J. Build. Eng.*, vol. 98, 2024, Art. no. 111061.

[17] Z. Tang et al., "Improving water pressure measurement using temperature-compensated wireless passive saw bidirectional RDL pressure sensor," *IEEE Trans. Instrum. Meas.*, vol. 71, 2021, Art. no. 9505111.

[18] S. Su, F. Xu, L. Zhang, S. Liu, and T. Ren, "Design and research of SIW wireless passive high-temperature and pressure sensor," *IEEE Sens. J.*, vol. 23, no. 22, pp. 27921–27930, Nov. 2023.

[19] M. Aslam, H. Zhang, V/ Sreejith, M. Naghdi, and S. Ju, "Advances in the surface acoustic wave sensors for industrial applications: Potentials, challenges, and future directions: A review," *Measurement*, vol. 222, 2023, Art. no. 113657.

[20] K. Liu et al., "Iontronic capacitance-enhanced LC wireless passive pressure sensor for high-performance flexible sensing," *Appl. Phys. Lett.*, vol. 123, no. 8, 2023, Art. no. 083501.

[21] L. Zhang et al., "Design of temperature-pressure sensor based on slot-antenna CSRR-integrated for applications in high-temperature environments," *IEEE Sensors J.*, vol. 24, no. 17, pp. 27218–27224, Sep. 2024.

[22] W. Guo et al., "Design of metamaterial high-temperature pressure sensor based on HTCC ceramic substrate," *IEEE Sensors J.*, vol. 25, no. 7, pp. 11176–11184., Apr. 2025.

[23] Z. Dong et al., "A dual-sensitive element wireless passive LC temperature sensor and application in bearing monitoring," *Meas. Sci. Technol.*, vol. 398, 2025, Art. no. 117299.

[24] Y. Wang, Y. Jia, Q. Chen, and Y. Wang, "A passive wireless temperature sensor for harsh environment applications," *Sensors*, vol. 8, no. 12, pp. 7982–7995, 2008.

[25] H. Kairm et al., "Concept and model of a metamaterial-based passive wireless temperature sensor for harsh environment applications," *IEEE Sensors J.*, vol. 15, no. 3, pp. 1445–1452, Mar. 2014.

[26] S. Timoshenko et al. *Theory of Plates and Shells*, vol. 2. New York, NY, USA: McGraw-Hill, 1959.

[27] M. A. Fonseca, J. M. English, M. Von Arx, and M. G. Allen, "Wireless micromachined ceramic pressure sensor for high-temperature applications," *J. Microelectromech. Syst.*, vol. 11, no. 4, pp. 337–343, 2002.

[28] H. Cheng et al., "Evanescent-mode-resonator-based and antenna-integrated wireless passive pressure sensors for harsh-environment applications," *Sensors Actuator A-Phys.*, vol. 220, pp. 22–33, 2014.

[29] Q. Tan, T. Luo, T. Wei, J. Liu, L. Lin, and J. Xiong, "A wireless passive pressure and temperature sensor via a dual LC resonant circuit in harsh environments," *J. Microelectromech. Syst.*, vol. 26, no. 2, pp. 351–356, 2017.

[30] J. E. Rogers, Y.-K/ Yoon, M. Sheplak, and J. W. Judy, "A passive wireless microelectromechanical pressure sensor for harsh environments," *J. Microelectromech. Syst.*, vol. 27, no. 1, pp. 73–85, 2017.

[31] Q. Tan, F. Lu, Y. Ji, H. Wang, W. Zhang, and J. Xiong, "LC temperature-pressure sensor based on HTCC with temperature compensation algorithm for extreme 1100° applications," *Sensors Actuator A-Phys.*, vol. 280, pp. 437–446, 2018.

[32] P. Jia, J. Liu, J. Qian, Q. Ren, G. An, and J. Xiong, "An LC wireless passive pressure sensor based on single-crystal MGO mems processing technique for high temperature applications," *Sensors*, vol. 21, no. 19, 2021, Art. no. 6602.

[33] M. Simone, M. B. Lodi, N. Curreli, S. C. Pavone, G. Mazzarella, and A. Fanti, "Optimized design and multiphysics analysis of a Ka-band stacked antenna for cubesat applications," *IEEE J. Multiscale Multiphys. Comput. Tech.*, vol. 6, pp. 143–157, 2021.

[34] K. Zhang and Y. An, "Research on multiphysics coupling relationship for the IPT system in seawater environment," *World Elect. Veh. J.*, vol. 12, no. 4, 2021, Art. no. 230.

[35] L. Huang et al., "Research on the multi-physics field coupling simulation of aero-rotor blade electrochemical machining," *Sci. Rep.*, vol. 11, no. 1, pp. 1–13, 2021.

[36] H. H. Zhang et al., "Electromagnetic-circuital-thermal multiphysics simulation method: A review," *Prog. Electromagn. Res.*, vol. 169, pp. 87–101, 2020.

[37] H. H. Zhang et al., "Parallel higher order DGTD and FETD for transient electromagnetic-circuital-thermal co-simulation," *IEEE Trans. Microw. Theory Tech.*, vol. 70, no. 6, pp. 2935–2947, Jun. 2022.

[38] C. T. Herakovich, *A Concise Introduction to Elastic Solids.* Berlin, Germany: Springer, 2017.

[39] P. A. Huidobro et al., "Magnetic localized surface plasmons," *Phys. Rev. X*, vol. 4, no. 2, 2014, Art. no. 021003.

[40] Z. Liao et al., "Localized surface magnetic modes propagating along a chain of connected subwavelength metamaterial resonators," *Phys. Rev. Appl.*, vol. 10, no. 3, 2018, Art. no. 034054.

[41] W. Tang, Y. Hua, and T. J. Cui, "A compact component for multi-band rejection and frequency coding in the plasmonic circuit at microwave frequencies," *Electronics*, vol. 10, no. 1, 2020, Art. no. 4.

[42] Y. Hua, W. Tang, and T. J. Cui, "A metamaterial sensor for detecting the location of a sub-wavelength object," *Appl. Phys. Lett.*, vol. 120, no. 18, 2022, Art. no. 181703 .

[43] M. Li et al., "High-temperature dielectric and microwave absorption properties of Si_3N_4–SiC/SiO_2 composite ceramics," *J. Mater. Sci.*, vol. 50, pp. 1478–1487, 2015.

[44] Y. Cheng, "The COMSOL Multiphysics model used in this study is publicly available on Zenodo: COMSOL Multiphysics model for wireless passive temperature and pressure sensors," Zenodo, 2025, doi: 10.5281/zenodo.17791012.

Yijia Cheng (Graduate Student Member, IEEE) received the B.S. degree in electronic information science and technology from Chongqing University, Chongqing, China, in 2021. She is currently working toward the Ph.D. degree in electronic science and technology from Zhejiang University, Hangzhou, China. Her research interests include computational nanophotonics, scattering matrix method, Fourier modal method, and higher-order topological photonics.

Yujie Hua (Graduate Student Member, IEEE) received the B.S. degree in radio wave propagation and antenna from the Tianjin University of Technology, Tianjin, China. He is currently working toward the Engineering Doctorate with the National Key Laboratory of Millimeter Waves, Southeast University, Nanjing, China. His research interests include wireless and passive multiphysics-field sensing, and including the principles, design, and applications of passive sensing technologies across electromagnetic, mechanical, and thermal domains.

Baiyun Wang received the B.Eng. degree from the School of Information Science and Engineering, Southeast University, Nanjing, China, where she is currently working toward the M.S. degree in electromagnetic fields and microwave technology. Her research focuses on the design and applications of metamaterial-based electromagnetic sensors.

Kang Wang received the B.E. degree from the North China University of Water Resources and Electric Power, Henan, China, in 2016. He is currently working toward the Ph.D. degree with Zhengzhou University, Zhengzhou, China. His research interests include polymer-derived ceramic thin-film sensing materials and their high-temperature thermo-/mechanical-electrical sensing applications.

Wenxuan Tang (Member, IEEE) received the B.Sc. and M.Sc. degrees from Southeast University, Nanjing, China, in 2006 and 2009, respectively, and the Ph.D. degree in electromagnetics from the Queen Mary University of London, London, U.K., in 2012. In 2012, she joined the School of Information Science and Engineering, Southeast University, where she is currently a Professor with the State Key Laboratory of Millimeter Waves. She has authored or coauthored more than 80 journal articles, one book, and two book chapters on metamaterials and their applications. Her research interests include metamaterials and their applications, and microwave devices and antennas.

Gang Shao received the B.S. and M.S. degrees in materials science and engineering from Zhengzhou University, Zhengzhou, China, in 2006 and 2009, and the Ph.D. degree in materials science and engineering from the University of Central Florida, Orlando, FL, USA, in 2013. From 2013 to 2014, he was a Lecturer with the School of Materials Science and Engineering, Zhengzhou University, where he was an Associate Professor from 2015 to 2019 and has been a Professor since 2020. He has led multiple national research projects and authored more than 200 journal papers in *Advanced Functional Materials*, *Journal of Materials Chemistry A*, *ACS Applied Materials & Interfaces*, and *Journal of Advanced Ceramics*, with several papers recognized as ESI highly cited. He also holds more than 15 Chinese invention patents and is also on the Editorial Boards of *Journal of Advanced Ceramics* and *International Journal of Applied Ceramic Technology*. His research interests include polymer-derived ceramics, sensors for extreme environments, and field-assisted ceramic processing. Dr. Shao was the recipient of the China Youth Science and Technology Innovation Award, Youth Science and Technology Award of the Chinese Ceramic Society, and Henan Provincial Outstanding Youth Fund.

Wei E. I. Sha (Senior Member, IEEE) received the B.S. and Ph.D. degrees in electronic engineering from Anhui University, Hefei, China, in 2003 and 2008, respectively. From 2008 to 2017, he was a Postdoctoral Research Fellow and a Research Assistant Professor with the Department of Electrical and Electronic Engineering, University of Hong Kong, Hong Kong. Between 2018 and 2019, he has held a Marie Skłodowska-Curie Individual Fellowship with University College London, London, U.K. In 2017, he joined the College of Information Science and Electronic Engineering, Zhejiang University, Hangzhou, China, where he is currently a tenured Associate Professor. He has authored or coauthored more than 200 peer-reviewed journal articles, 180 conference papers, 12 book chapters, and two books. His work has been cited more than 11,700 times on Google Scholar, with an H-index of 58. His research interests include theoretical and computational electromagnetics, computational and applied electromagnetics, nonlinear and quantum electromagnetics, micro- and nano-optics, and multiphysics modeling. He has reviewed for more than 60 technical journals and served on the Technical Program Committees of more than ten IEEE conferences. He is also an Associate Editor for IEEE JOURNAL ON MULTISCALE AND MULTIPHYSICS COMPUTATIONAL TECHNIQUES, IEEE OPEN JOURNAL OF ANTENNAS AND PROPAGATION, IEEE ACCESS, and *Electromagnetic Science*. Dr. Sha was the recipient of the multiple awards, including the ACES-China Electromagnetics Education Ambassador Award (2024), ACES Technical Achievement Award (2022), and PIERS Young Scientist Award (2021), and also Nine of his students have won Best Student Paper Awards. He is also a Life Member of OSA.